

Three-Dimensional Graphene Field-Effect Transistors as High-Performance Photodetectors

Tao Deng,*^{†,‡,§} Zhaohao Zhang,^{‡,||} Yaxuan Liu,[†] Yingxin Wang,^{§,¶} Fang Su,[†] Shasha Li,[†] Yang Zhang,[†] Hao Li,[†] Houjin Chen,[†] Ziran Zhao,[§] Yue Li,^{†,‡} and Zewen Liu^{*}

[†]School of Electronic and Information Engineering, Beijing Jiaotong University, Beijing 100044, China

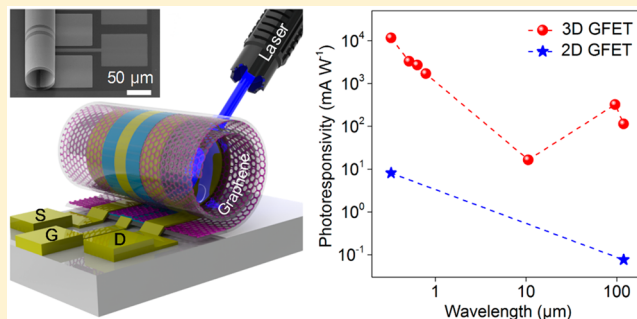
[‡]Institute of Microelectronics, [§]Key Laboratory of Particle & Radiation Imaging, Ministry of Education, Department of Engineering Physics, and ^{||}Department of Electronic Engineering, Tsinghua University, Beijing 100084, China

[¶]Key Laboratory of Microelectronics Devices & Integrated Technology, IC Advanced Process R&D Center, Institute of Microelectronics of Chinese Academy of Sciences (IMECAS), Beijing 100029, China

Supporting Information

ABSTRACT: Graphene is an ideal material for high-performance photodetectors because of its superior electronic and optical properties. However, graphene's weak optical absorption limits the photoresponsivity of conventional photodetectors based on planar (two-dimensional or 2D) back-gated graphene field-effect transistors (GFETs). Here, we report a self-rolled-up method to turn 2D buried-gate GFETs into three-dimensional (3D) tubular GFETs. Because the optical field inside the tubular resonant microcavity is enhanced and the light–graphene interaction area is increased, the photoresponsivity of the resulting 3D GFETs is significantly improved. The 3D GFET photodetectors demonstrated room-temperature photodetection at ultraviolet, visible, mid-infrared, and terahertz (THz) regions, with both ultraviolet and visible photoresponsivities of more than 1 A W^{-1} and photoresponsivity of 0.232 A W^{-1} at 3.11 THz. The electrical bandwidth of these devices exceeds 1 MHz. This combination of high photoresponsivity, a broad spectral range, and high speed will lead to new opportunities for 3D graphene optoelectronic devices and systems.

KEYWORDS: 3D, graphene, FET, photodetector, THz



Photodetectors are essential elements in many applications, including optical communications, imaging, and sensing.^{1,2} Graphene has emerged as a promising material for the fabrication of high-performance photodetectors because of its gapless bandstructure, ultrafast carrier dynamics, and optical properties that can be tuned via electrostatic doping.² Early graphene-based photodetectors generally adopted planar (2D) back-gated graphene field-effect transistor (GFET) structures.^{3,4} Using the photovoltaic effect^{5,6} and the photothermoelectric effect,^{7,8} 2D GFET-type photodetectors can operate over a broad spectrum and at very high frequencies (~40 GHz).³ However, the photoresponsivities of these 2D GFET photodetectors are limited to a few mA W⁻¹ because single-layer graphene can absorb only 2.3% of the incident light.⁹ Integrating graphene with plasmonic nanostructures can enhance the responsivity of the photodetectors, but the enhancement only occurs at the designed wavelength.^{10,11} Silicon waveguide-integrated graphene photodetectors demonstrated relatively broadband photodetection with modestly increased photoresponsivities.^{12–14} By combining graphene with other photosensitive materials, such as quantum dots (QDs),^{15,16} carbon nanotubes,¹⁷ or another layer of graphene¹⁸ to form hybrid

systems, the responsivity of the photodetectors can be dramatically enhanced. For example, hybridized graphene-QD photodetectors based on the photogating effect have achieved extremely high photoresponsivities of $\sim 10^9 \text{ A W}^{-1}$,¹⁶ however, the photoresponses were very slow, with electrical bandwidths of approximately 1–10 Hz.¹⁵

An alternative approach to enhancing the photoresponsivity and simultaneously maintaining the ultrafast response speed of graphene photodetectors is to integrate them with optical resonant microcavities. Furchi et al. demonstrated that by integrating graphene with a planar Fabry–Perot microcavity consisted of two distributed Bragg mirrors, the optical absorption was 26-fold enhanced.¹⁹ The Bragg mirrors can also be replaced by metal mirrors.²⁰ The main drawback of such planar microcavity-integrated graphene photodetectors is that the photoresponsivity enhancement can only be achieved at the designed resonant frequencies. To solve this problem, three-dimensional (3D) tubular optical microcavities fabricated by the

Received: October 12, 2018

Revised: January 29, 2019

Published: January 30, 2019

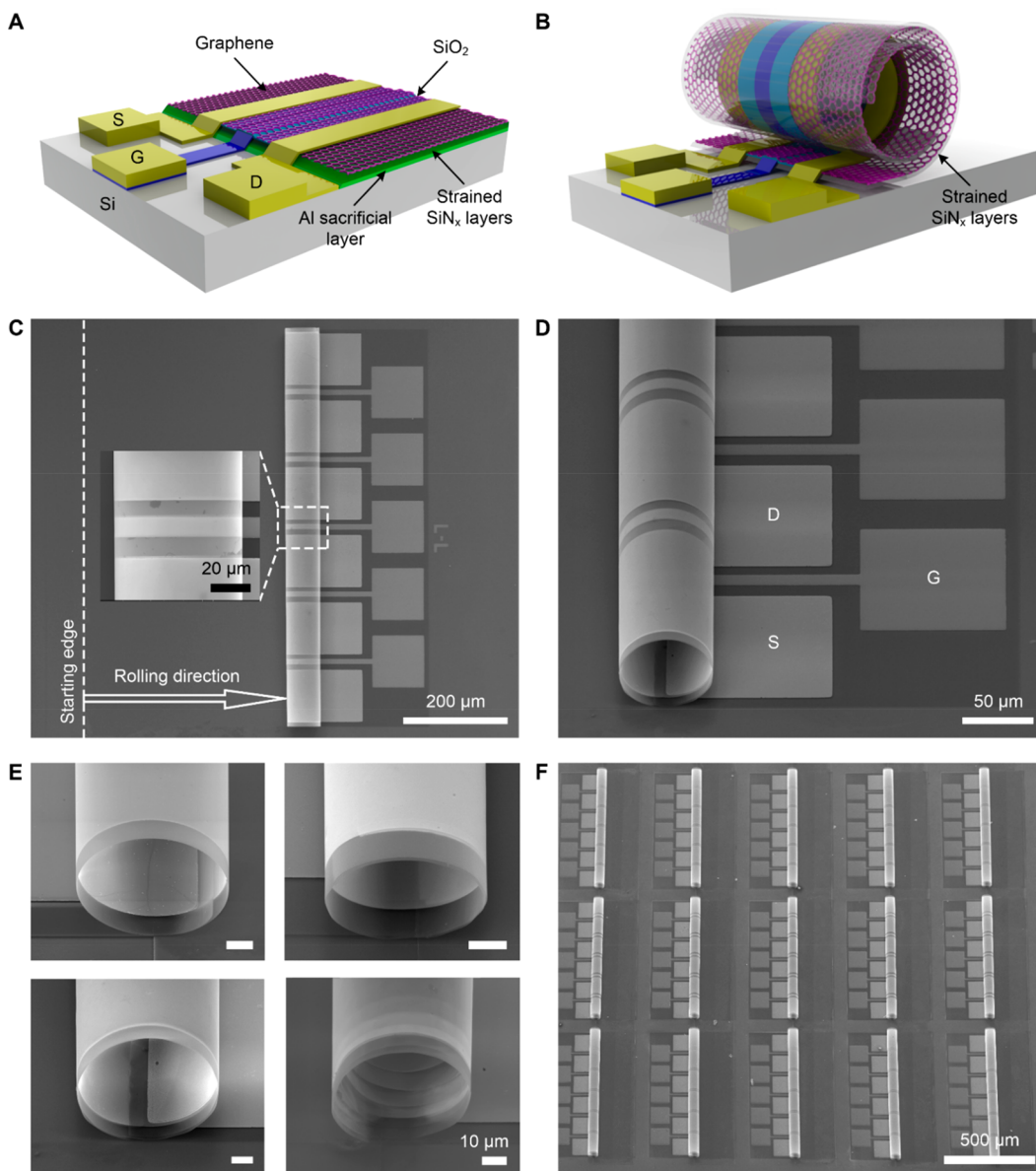


Figure 1. Structure and SEM images of the rolled-up 3D GFETs. (a, b) Schematic diagrams of the 2D GFETs and 3D GFETs before and after the roll-up process, respectively. (c, d) Top view and side view of a 3D GFET. The inset in panel c shows a close-up of the graphene conductive channel of the 3D GFET. (e) Side views of four 3D GFETs with a single winding (top left corner), two windings (top right corner), three windings (bottom left corner), and five windings (bottom right corner). The scale bars represent 10 μm . (f) Array of 3D GFET tubes.

self-rolled-up technology²¹ can be used. Self-rolled-up InGaAs/GaAs tubular microcavities have been used to enhance the responsivity of InAs QD photodetectors.^{22,23} Recently, Wang et al. proposed a 3D quantum-well infrared photodetector (QWIP) based on self-rolled-up GaAs/AlGaAs QW-embedded microtubes.²⁴ The 3D QWIP presented a light-trapping enhancement (~3 times) of the photoresponsivity over a broad wavelength range from 3 to 8 μm at a temperature of 60 K.²⁴ In fact, self-rolled-up graphene/Cr/InGaAs microtubes without any electrode and graphene/SU-8 tubular diodes have been realized by Barcelos et al.²⁵ and our group,²⁶ respectively. However, the fabrication and optical applications of the self-rolled-up GFET have not been addressed to date.

Here, a self-rolled-up 3D GFET photodetector was demonstrated to balance its photoresponsivity, spectral range, and electrical bandwidth for the first time. The multiwinding 3D GFET not only provides a natural resonant microcavity to

enhance the optical field but also increases the light–graphene interaction area, resulting in significantly enhanced optical absorption. Thus, the photoresponsivity of the 3D GFET was significantly improved. Simultaneously, the intrinsic ultrafast and ultra-broadband photoelectronic properties of graphene were maintained.

Inspired by the tubular InGaAs/GaAs FETs reported by Schmidt et al.,²⁷ the 3D GFETs were fabricated using the following process. First, after a 50 nm thick Al sacrificial layer was sputtered on the Si substrate, a compressively strained SiN_x layer and a tensile strained SiN_x layer were deposited successively using low-frequency (380 kHz) and high-frequency (13.56 MHz) plasma-enhanced chemical vapor deposition (PECVD) processes, respectively.²⁸ Variation of the thicknesses of these compressively strained and tensile strained SiN_x layers allows the diameter of the tubular 3D GFET to be tuned precisely. Second, a Cr/Au (10 nm/30 nm) gate electrode

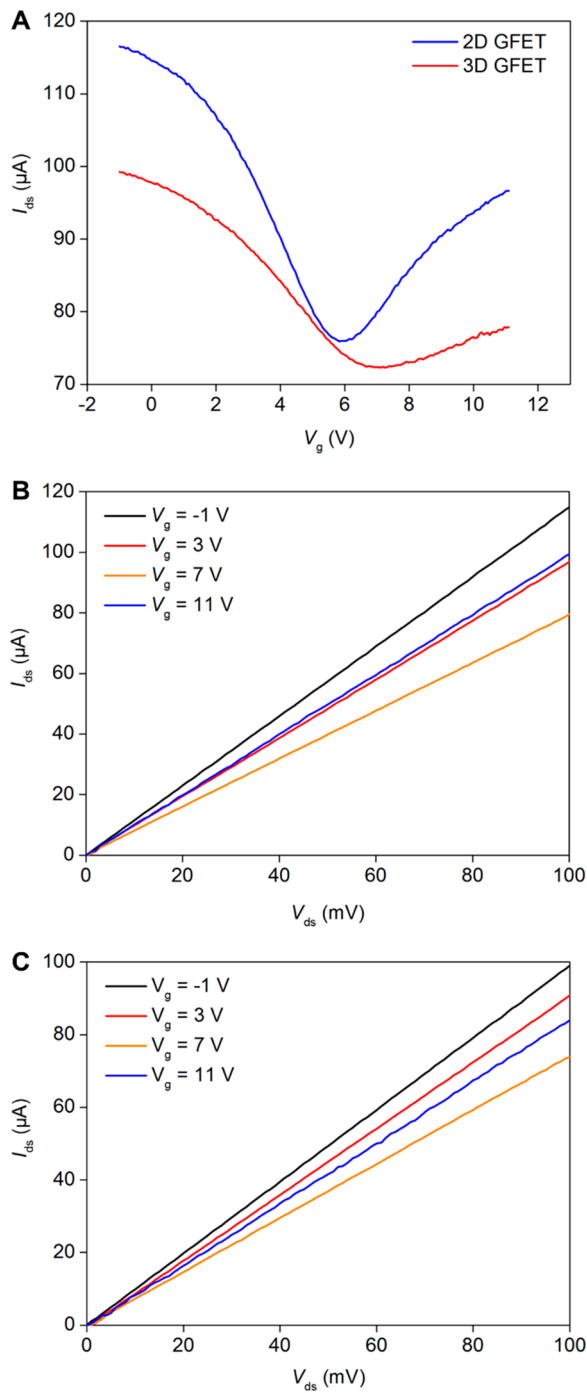


Figure 2. Electrical properties of GFET before (2D) and after (3D) the roll-up process. (a) Transfer characteristic curves of the GFET as a function of gate voltage (V_g) in the 2D (blue line) and 3D (red line) states. The source-drain voltage (V_{ds}) was fixed at 100 mV. Output characteristic curves of (b) the 2D GFET and (c) the 3D GFET as functions of the source-drain voltage for various gate voltages.

structure was sputtered on the SiN_x layers, with subsequent deposition of a 30 nm thick SiO_2 dielectric layer on top. Third, monolayer CVD-grown graphene (ACS Material, LLC) was transferred onto the SiO_2 layer and patterned using oxygen plasma etching. Fourth, after evaporation of the Cr/Au (10 nm/50 nm) source and drain electrodes, the 2D buried-gate GFET was formed (Figure 1a). Then, following selective etching of the underlying Al sacrificial layer using a FeCl_3 solution, the strained

SiN_x layers caused the 2D GFET to roll up. Finally, after washing and drying stages, the 3D GFET was complete (Figure 1b). A detailed description of the fabrication process can be found in Figure S1.

Figure 1c shows a 3D GFET tube rolled up from a 2D buried-gate GFET with graphene conductive channel dimensions of $30 \mu\text{m} \times 400 \mu\text{m}$ (length \times width). The chip area of the 3D GFET is much smaller than that of the 2D GFET. A magnified image of the graphene conductive channel (see the inset in Figure 1c) indicates that the 3D GFET is well-constructed. From the side-view of the 3D GFET (Figure 1d), the diameter is 60 μm , and the rolled-up winding number is about three. The tight contact between consecutive windings can be seen in the higher magnification image in the bottom left corner of Figure 1e. By varying the thicknesses of the compressively and tensile strained SiN_x layers and changing the device dimensions, various 3D GFETs with different winding numbers (from 1 to 5) and different diameters (30 μm –65 μm) were obtained, as shown in Figures 1e and S2. The top rolled-up layer (containing the source and drain electrodes) of the inner winding is in contact with the released bottom surface (SiN_x layers), and the SiN_x layers thus provide natural electrical insulation between the adjacent windings in the 3D GFET tube. Figure 1f shows a 5×3 array of microtubes containing 5 parallel 3D GFETs each, which indicates that high-density 3D GFETs can be fabricated controllably on a very large scale, which is important for practical applications such as imaging and sensing.²

The 3D GFETs were characterized using Raman spectroscopy to confirm the presence of the graphene layer in the rolled-up state (Figure S3). The electrical properties of the 2D and 3D GFETs were investigated using a semiconductor parameter analyzer (B1500A, Keysight Tech.) and a probe station (Summit 12000, Cascade Microtechnology) at room temperature. Figure 2a shows the transfer characteristic curves of a typical GFET before and after the roll-up process. Both the 2D GFET and the 3D GFET show typical ambipolar characteristics. The Dirac point (V_{Dirac}) of the 2D GFET, which is defined as the gate voltage (V_g) at which the minimum source-drain current (I_{ds}) is obtained, occurs at 6 V, which indicates that the graphene is p-doped. The Dirac point of the 3D GFET, however, has shifted to 7 V. One possible reason for this Dirac point shift is the adsorption of water molecules from the etching solution used for the Al sacrificial layer in the roll-up process.²⁹ It is worth noting that the Dirac points of the 2D GFET and 3D GFET are much smaller than that of previous reported back-gated 2D GFETs (~ 30 V) using thermal oxide (SiO_2) as gate dielectric layers^{18,30} because the thickness of the SiO_2 dielectric layer in our devices is only 30 nm, while those in the back-gated 2D GFETs are up to 300 nm.^{18,30} When compared to the transconductance of the 2D GFET in the linear region, the transconductance of the 3D GFET in the linear region decreases significantly. To figure out the reason, the field effect mobility (μ) and metal–graphene contact resistance (R_{contact}) of the GFETs before and after the roll-up process were quantitatively investigated. For the 2D GFET (Figure S4a), $\mu = 1070 \text{ cm}^2/(\text{V s})$, which is comparable to that of reported back-gated 2D GFETs,³⁰ and $R_{\text{contact}} = 676 \Omega$. After the roll-up process, the hole mobility decreases to $\mu = 780 \text{ cm}^2/(\text{V s})$, and the contact resistance increases to $R_{\text{contact}} = 804 \Omega$, as shown in Figure S4b. Both the decrease of μ and the increase of R_{contact} result in a lower transconductance. Therefore, the transconductance of the 3D GFET in the linear region is significantly lower than that of the 2D GFET. Detailed

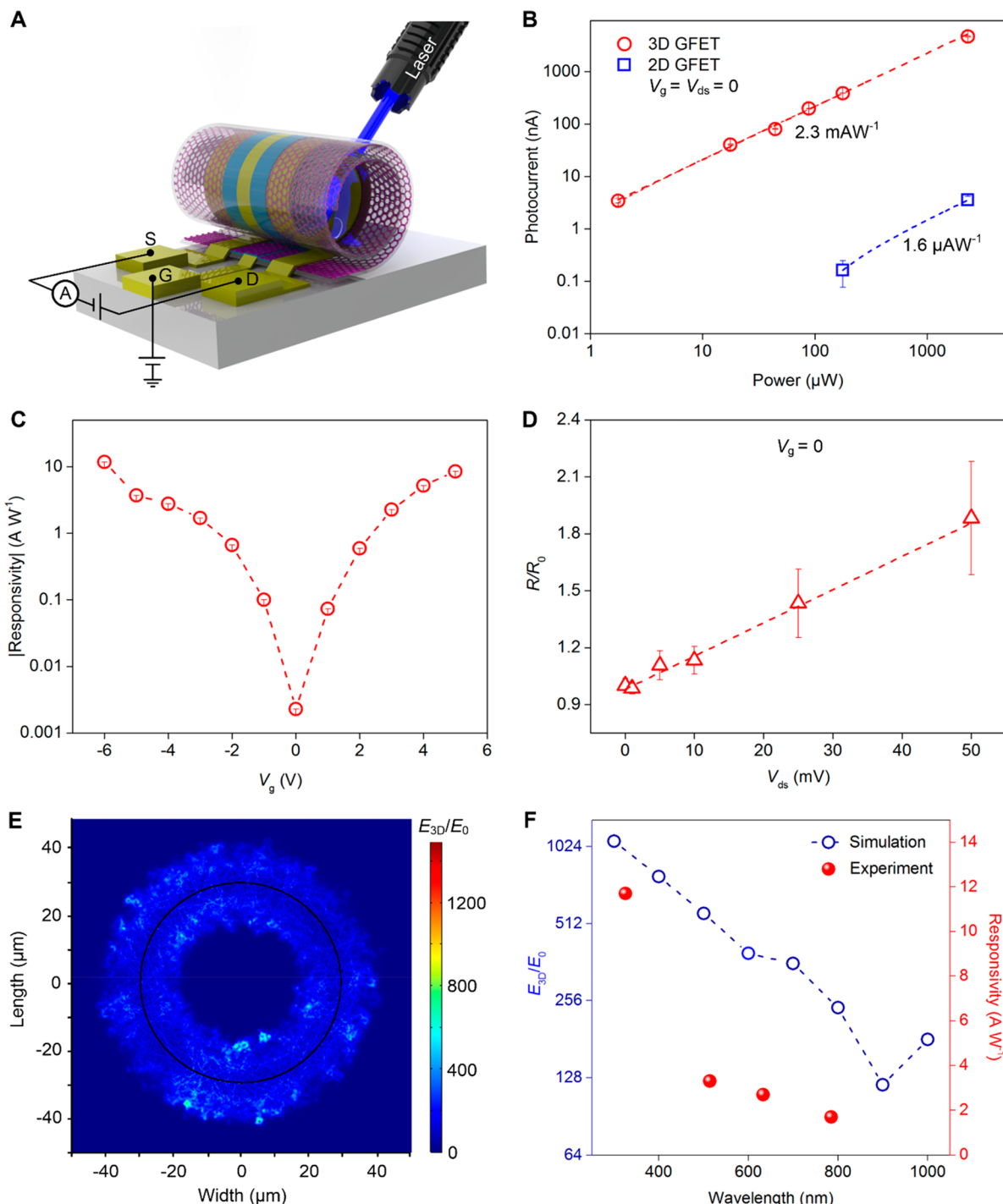


Figure 3. Photoresponses of the 2D GFETs and 3D GFETs in the ultraviolet and visible regions. (a) Schematic showing the experimental setup. (b) Measured photocurrent with respect to incident ultraviolet laser power for the 2D GFETs and 3D GFETs under zero gate bias ($V_g = 0 \text{ V}$) and zero source-drain bias ($V_{ds} = 0 \text{ V}$) conditions. (c) Gate-voltage-dependent responsivity of the 3D GFETs under $V_{ds} = 0 \text{ V}$. (d) Responsivity (R) enhancement factor (R/R_0 , where R_0 is the original R under conditions of $V_g = V_{ds} = 0 \text{ V}$) of the 3D GFETs vs V_{ds} under $V_g = 0 \text{ V}$. The ultraviolet laser wavelength was 325 nm, and the spot size was approximately 2 μm . (e) The simulated distribution of the electric field magnitude near a 3D GFET with only one rolled-up winding, under illumination by a surface light source with a wavelength of 514 nm and an electric field magnitude of $E_0 = 1 \text{ V/m}$. (f) The average relative electric field magnitude (E_{3D}/E_0) at the interior surface of the 3D GFET and the measured photoresponsivity of the 3D GFETs, where both quantities change with the wavelength of the incident light. All measurements were performed at room temperature.

information about the analysis can be found in the Supporting Information.

The output characteristic curves of the 2D GFET are shown in Figure 2b. With increasing source-drain voltage (V_{ds}), the output source-drain current (I_{ds}) increases linearly. At a specific

V_{ds} , the output current first decreases and then increases with increasing gate voltage from -1 to 11 V, thus indicating good gate-control ability. Similar tendencies can be seen in the output characteristic curves of the 3D GFET, as shown in Figure 2c. It should be noted that the output current of the 3D GFET is

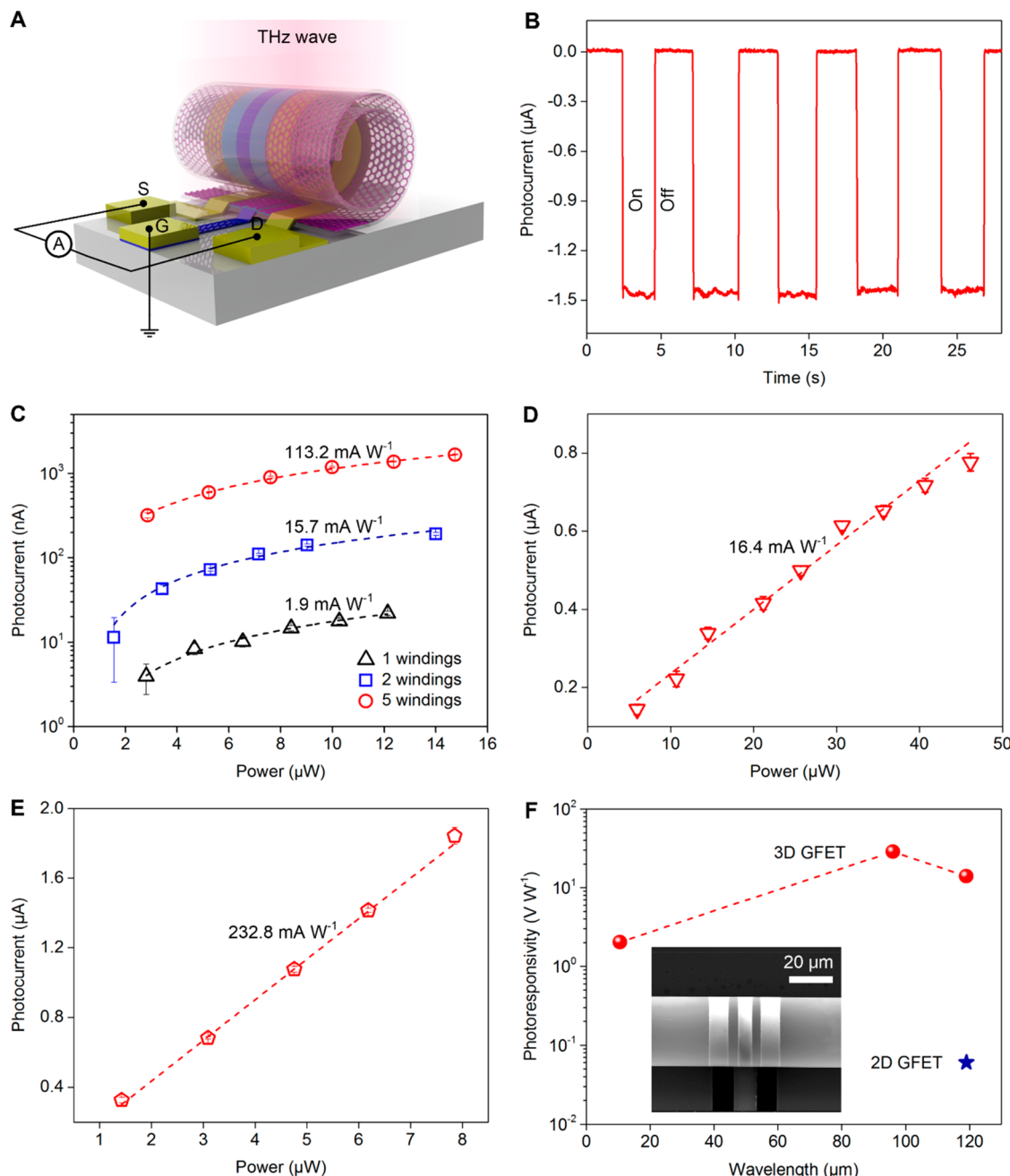


Figure 4. Photoresponses of the 3D GFETs in the mid-infrared and THz regions. (a) Schematic of the experimental setup. (b) Temporal photocurrent response of a 3D GFET with five rolled-up windings under excitation by a 119 μm (2.52 THz) laser. (c) Measured photocurrent with respect to incident laser (119 μm) power for 3D GFETs with different numbers of windings. (d, e) Measured photocurrent with respect to incident laser power at wavelengths of 10.6 and 96 μm (3.11 THz), respectively, for 3D GFETs with five windings. (f) Voltage photoresponsivities of 2D GFETs (blue star) and 3D GFETs with five windings (red circles) with respect to wavelength. The inset shows the 3D GFET used to obtain the data. The spot sizes of the mid-infrared and THz lasers were approximately 3 mm and 1.5 mm (FWHM), respectively. All measurements were performed at room temperature and under zero gate bias ($V_g = 0 \text{ V}$) and zero source-drain bias ($V_{ds} = 0 \text{ V}$).

smaller than that of the 2D GFET under the same gate and source-drain voltages. This phenomenon indicates that the GFET's resistance increases after the roll-up process. It has previously been reported that crumpled,³¹ folded,³² and rolled²⁶ graphene structures have shown increased resistance, which is consistent with our observations. A possible method to improve the electrical properties of the 3D GFETs is to replace the single-layer graphene with stacked multiple graphene layers. Barcelos et al. rolled stacked multiple graphene layers into microtubes using an InGaAs-Cr strain system and found that no layer-to-

layer registry (graphitization) was formed in the rolled-up stacked graphene layers.³³ Compared with rolled-up GFETs based on single-layer graphene, the rolled-up GFETs based on stacked multiple graphene layers are expected to have many advantages, such as lower sheet resistance of the graphene channel, lower graphene–metal contact resistance, and higher hole carrier mobility.^{34,35} However, the Dirac point (V_{Dirac}) may shift to the positive V_g direction as the number of the stacking graphene layers increases because of the accumulation of negative charges and moisture trapped in the graphene during

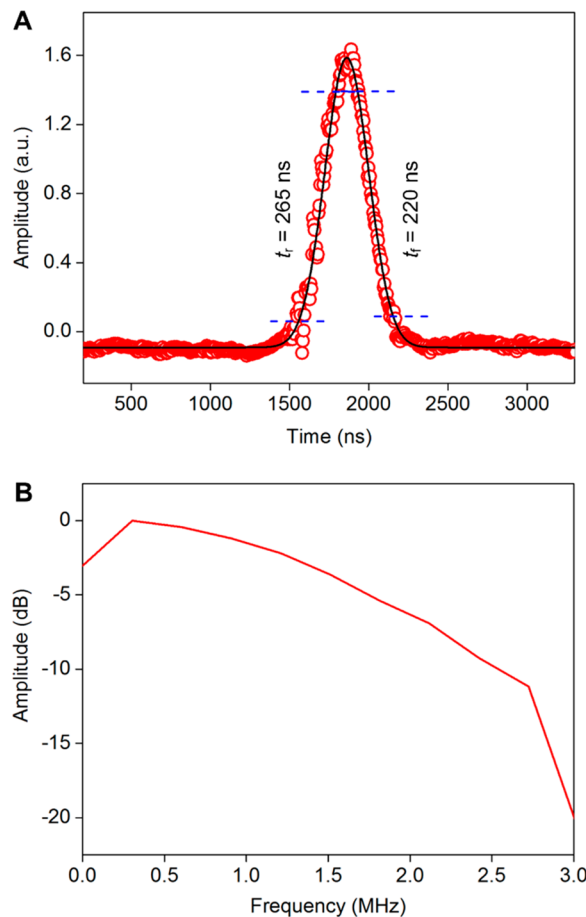


Figure 5. High-speed photoresponse of the 3D GFETs. (a) Impulse response of the device amplified using a low-noise current preamplifier (with 1 MHz bandwidth) and recorded using a 1 GHz bandwidth sampling oscilloscope, showing the rise time (t_r) and the fall time (t_f). The rise and fall times were defined as the signal increasing or decreasing from 10% or 90% to 90% or 10% of the stable signal, respectively. (b) Frequency response obtained via discrete time Fourier transform of the time-domain data. The 3 dB bandwidth is approximately 1.38 MHz; a.u.: arbitrary units.

the layer-by-layer transfer process.³⁶ Figure S5 shows that the gate leakage current of the 3D GFET is about 10 pA, which is comparable with typical 2D GFETs,^{37,38} indicating that the gate leakage current is negligible.

After they were diced into smaller chips, the 3D GFETs were bonded to printed circuit boards (Figure S6). The photoelectric properties of these 3D GFETs in the ultraviolet region (325 nm) were characterized and compared with those of reference 2D GFETs with the same graphene conductive channel dimensions using the experimental setup shown in Figure 3a. The laser beam with a spot size of $\sim 2 \mu\text{m}$ was generated using a laser confocal Raman spectrometer (LabRam HR-800, Horiba Jobin Yvon). A source meter (2400, Keithley) was used to apply the gate bias to the devices, and a precision source/measure unit (B2911A, Agilent) was used to supply the source-drain bias voltage and detect the source-drain current of the devices. By performing a scanning photocurrent experiment,³⁹ we found that the photocurrent exhibited significant enhancement at the graphene-metal contacts and opposite sign for the two junctions, as shown in Figure S7. This phenomenon indicates that photovoltaic (PV) and photothermoelectric (PTE) effects rather than photogating effect play a major role in the photocurrent

generation; if photogating dominates the response, then the photocurrent would be mainly generated in the channel center.⁴⁰ Figure 3b shows the laser power dependence of the photocurrent of a 3D GFET with 2 windings and a reference 2D GFET under zero gate bias and zero source-drain bias. The 3D GFET's photocurrent rises linearly with increasing incident laser power. The responsivity (R), which is defined as the ratio of the measured photocurrent to the input laser power, is 2.3 mA W^{-1} . This responsivity is 3 orders of magnitude higher than that of the reference 2D GFET ($1.6 \mu\text{A W}^{-1}$). Similar responsivity enhancements were also observed in the visible region (514, 633, and 785 nm), as shown in Figure S8. These phenomena are mainly caused by the enhancement of the optical field inside the tubular microcavity and the increased light-graphene interaction area of the 3D GFET. Besides, the suspended GFET structure also eliminates a dominant electronic cooling channel via the surface phonons of the polar substrate.⁴¹

Figure 3c shows the gate-voltage-dependent photoresponsivity of the 3D GFET under 325 nm laser excitation. The photoresponsivity rises sharply with an increase in the absolute gate voltage value and changes sign at a gate voltage of about 0 V (defined as V_{FB}). The V_{FB} signifies the flat-band conditions in which the electron band near the metal–graphene contact is level (thus no electric field). It is worth noting that the V_{FB} of the 3D GFET photodetector is on the left side of the Dirac point ($V_{Dirac} = 7 \text{ V}$). This phenomenon is related to the work functions of the metal electrode and of graphene and the Fermi level shift imparted by the metal doping on the graphene sheet.⁴² In the back-gated 2D GFET photodetectors with Cr/Au electrodes, Cai et al.⁴³ and Park et al.³⁹ also observed that V_{FB} s were on the left side of V_{Dirac} s, and the difference between V_{FB} and V_{Dirac} ($V_{FB} - V_{Dirac}$) could be as large as -20 V . Importantly, the gate voltage modulation of the photoresponsivity of the 3D GFETs is much stronger than the corresponding characteristic in conventional 2D back-gated GFET photodetectors^{3,43} because of their unique multiwinding gate structure and thin gate oxides.⁴ When the gate voltage increases from 0 to 1 V, the photoresponsivity then increases by almost 2 orders of magnitude. With further increases in the gate voltage, the rate at which the photoresponsivity increases is gradually reduced. However, photoresponsivities of more than 1 A W^{-1} can be obtained when the gate voltage exceeds 3 V; this is 2 orders of magnitude higher than the photoresponsivity of the conventional 2D back-gated GFET photodetectors (a few millamps per watt).^{3,4} The photoresponsivity of the 3D GFET can also be modulated by applying a back gate voltage to the Si substrate, as shown in Figure S9. Unlike typical back-gated 2D GFET photodetectors,^{10,44} where the graphene and dielectric layers have tight contact with the Si substrate (namely the back gate), the tubular graphene/dielectric/ SiN_x layers of the 3D GFET are suspended from the surface of the Si substrate. Thus, the photoresponsivity modulation by application of a back gate bias voltage is relatively small.

The photoresponsivity of the 3D GFETs can be enhanced by application of a source-drain bias voltage (see Figure 3d), but the fluctuations also increase because of the enhanced dark current that occurs in the graphene.⁴ Surprisingly, the photoresponse of the 3D GFET exhibits significant polarization dependence, as shown in Figure S10. A signal intensity ratio of ~ 1.2 is observed between the parallel and perpendicular polarizations with the maximum intensity occurring for the polarization direction parallel to the tube axis of the 3D GFET. This phenomenon might be analogous to that observed in highly

Table 1. Optoelectronic Characteristics of Typical Photodetectors Based on Graphene and Other Two-Dimensional Materials

ref	description	wavelength	responsivity (A/W)	detectivity (Jones)	NEP (pW Hz ^{-1/2})	response speed
12 and 13	graphene-Si waveguide	1.3–2.75 μm	0.13	—	—	25 ps
18	graphene-Ta ₂ O ₅ -graphene heterostructure	0.5–3.2 μm	>1	—	~10	~1 s
43	graphene with dissimilar metal contacts	1.54 μm, 119 μm	>10 V W ⁻¹	—	1100	~30 ps
53	lateral graphene p–n junction	532–1550 nm	1.4–4.7	~10 ¹²	—	~0.8 μs
47	graphene-coupled antenna	8–220 μm	5–10 × 10 ⁻⁹	—	—	10 ps, 50 ps
16	B-doped Si-QD/graphene phototransistor	UV-MIR	~10 ⁹ (UV-NIR), ~ 44.9 (MIR, 77K)	10 ¹³ (UV-NIR), ~ 10 ⁵ (MIR)	10 ⁻⁶ (UV-NIR), ~ 10 ² (MIR)	~3.4–9.0 s
54	multilayer MoS ₂ with metal electrodes	455–2717 nm	0.051–0.029	1.55–0.88 × 10 ⁹	—	—
55	b-P FET	532 nm– 3.39 μm	1000–82	—	~5.6	0.13 ms
40	b-AsP phototransistor, b-AsP/MoS ₂ heterostructure	2.4–8.05 μm	~0.03 (b-AsP), 0.22 (b-AsP/MoS ₂)	1.06 × 10 ⁸ (b-AsP), 9.2 × 10 ⁹ (b-AsP/MoS ₂)	≤4.35 (b-AsP), ≤ 0.24 (b-AsP/MoS ₂)	0.52 ms
56	b-PC phototransistor	2004 nm	~2163	~10 ¹¹	1.3 × 10 ⁻³	~0.7 ns (tunable)
51	WSe ₂ –In ₂ O ₃ NW phototransistor	visible-NIR	7.5 × 10 ⁵ (637 nm), 3.5 × 10 ⁴ (940 nm)	4.17 × 10 ¹⁷ (637 nm) 1.95 × 10 ¹⁶ (940 nm)	—	~20 ms
this work	3D graphene FET	UV, visible, MIR, THz	>1 (UV, visible), 0.23 (96 μm)	2.8 × 10 ¹⁰ (96 μm)	48 (96 μm)	~265 ns

aligned carbon nanotube photodetectors and can be attributed to the polarization-dependent absorption.^{45,46} The result indicates that the 3D GFETs have some potential for polarization determination.

To investigate the photoresponsivity enhancement mechanism for these 3D GFETs, the optical field (the electromagnetic field) near the 3D GFETs was simulated by the finite element method (FEM) using the commercial Comsol Multiphysics software. Figure 3e shows the electric field magnitude distribution near a 3D GFET with only one rolled-up winding, under illumination by normally incident light at a wavelength of 514 nm and an electric field magnitude of $E_0 = 1$ V/m. Because the tubular architecture provides an ingenious microcavity, the incident light resonates close to the interior and exterior surfaces of the 3D GFET using an evanescent mode, i.e., the electric field magnitude decreases exponentially with increasing distance away from the surfaces. The average relative electric field magnitude (E_{3D}/E_0) at the interior surface of the 3D GFET approaches a value of 500, which is much higher than the electric field enhancement factor that was obtained using a planar Fabry–Perot microcavity.¹⁹ Additionally, unlike planar optical resonant microcavities that only allow field enhancement at a designed wavelength, the tubular microcavity of the 3D GFET enhances optical fields over the range from the ultraviolet region to the visible region, as shown in Figure 3f. As the incident light wavelength increases from 300 to 1000 nm, E_{3D}/E_0 decreases before 900 nm, and then increases slightly. It is obvious that the higher electric field magnitude at the 3D graphene surface allows more energy to be absorbed, which then leads to the higher photoresponsivity. The experimental photoresponsivities of the 3D GFETs demonstrated similar tendencies to the simulation results (Figure 3f). Furthermore, the tube diameter and the winding number of the 3D GFET also affect E_{3D}/E_0 , as illustrated in Figure S11. By properly choosing the tube diameter of the 3D GFET, the photoresponsivities in the ultraviolet and visible regions can be enhanced over 1 order of magnitude (Figure S12). The relative photoresponsivities of the 3D GFET at different wavelengths also change with the tube diameter,

indicating that the tube diameter can be tuned to favor a specific wavelength range above other spectral intervals.

The 3D GFETs were also tested under both mid-infrared (10.6 μm) and terahertz (2.52 THz and 3.11 THz) illuminations using the experimental setup shown in Figure 4a. The 10.6 μm laser beam with a spot diameter of 3 mm was generated by a CO₂ laser (model CCL-II CO₂, Cosmetic Laser), while the 2.52 THz (119 μm) and 3.11 THz (96 μm) laser beams with a spot size (full width at half-maximum, FWHM) of 1.5 mm were provided by a far-infrared gas laser (FIRL 100, Edinburgh Instruments Ltd.). The laser spot sizes of these mid-infrared and THz laser beams were much larger than the dimensions of the 3D GFETs. Therefore, when the photoresponsivities were calculated, only the portion of the incident light intensity that overlapped with the device was used. All of the experiments were performed at room temperature and under zero gate bias and zero source-drain bias conditions. Figure 4b shows a typical on–off photocurrent characteristic of a 3D GFET under illumination by an incident laser (119 μm) power (on the 3D GFET) of 12.8 μW. After hundreds of on–off cycles, the photocurrent level is maintained well, thus indicating the good reliability and reversibility of these 3D GFETs. When the incident power increased to 14.5 μW, a very weak photocurrent (~1.5 nA) was observed in the reference 2D GFETs (Figure S13); this current was 3 orders of magnitude lower than that in the 3D GFET. The temporal photoresponse of the 3D GFET at other wavelengths within the mid-infrared and THz regions are shown in Figure S13.

Figure 4c shows a plot of the power dependence of the photocurrent for 3D GFETs with different numbers of rolled-up windings. Based on a 3D GFET with only one winding, a photoresponsivity of 1.9 mA W⁻¹ was obtained at a wavelength of 119 μm. When the number of windings of the 3D GFET was increased from 1 to 2, the photoresponsivity then also increased to 15.7 mA W⁻¹. When the number of windings increased continuously to 5, an amazing photoresponsivity of 113.2 mA W⁻¹ was achieved. With the increase of the winding number, the graphene–light interaction area increases, while the electrical resistance of the device decreases, both of which lead to

enhanced photocurrent (photoresponsivity). Furthermore, the relative positions of the electrodes in different windings shift slightly after the roll-up process, and the shift amount becomes larger when the winding number gets bigger, as shown by the red arrows in the inset of Figure S2c. The shifts of electrode relative positions may introduce asymmetry in the electrodes or device shape, which is of importance to produce a net photocurrent via the thermoelectric effect.⁴³ Another possible contributing factor is that the optical field inside the tubular microcavity changes with the winding number. Using these five-winding 3D GFETs, photoresponsivities of 16.4 and 232.8 mA W⁻¹ were obtained at wavelengths of 10.6 and 96 μm, respectively, as shown in Figure 4d,e. This data (232.8 mA W⁻¹ at 3.11 THz) is 7 orders of magnitude higher than that (5 nA W⁻¹) obtained for a 2D single-layer graphene THz photodetector coupled with antennas⁴⁷ and over 2 orders of magnitude higher than that (1.3 mA W⁻¹) obtained for a 2D double-layer graphene FET THz photodetector coupled with antennas⁴⁸ operating in the same photocurrent mode. In addition, the photoresponsivity of the 3D GFETs in the THz region can be tuned by applying gate biases (Figure S14).

The theoretical estimation of the room temperature Johnson–Nyquist noise floor, given by $(4k_B T R_{\text{total}})^{1/2}$, is 1.4 nV (Hz)^{-1/2}, where k_B is the Boltzmann constant, T is the temperature, and R_{total} is the measured resistance. The noise-equivalent power (NEP) of the photodetector can be calculated using the ratio of the noise voltage to the voltage photoresponsivity.^{42,49} The voltage photoresponsivity of the 3D GFETs was 28.9 V W⁻¹ (at 3.11 THz) under zero gate bias conditions (Figure 4f), which was obtained by multiplying the current photoresponsivity by the measured device resistance (124 Ω for 5-winding 3D GFETs). Using this method, the NEP of the 3D GFET photodetectors at 3.11 THz is expected to be approximately 48 pW (Hz)^{-1/2}, which is 1 order of magnitude higher than that obtained for single-layer graphene-based THz detectors,^{42,49} and is comparable to that for conventional THz detectors based on complementary metal-oxide-semiconductor FETs (CMOSFETs; 85 pW (Hz)^{-1/2}).⁵⁰ Assuming that the shot noise from the dark current is a major contribution, the specific detectivity (D^*) can be calculated using $D^* = RA^{1/2}/(2eI_{\text{dark}})^{1/2}$, where R is the photocurrent responsivity, A is the effective photoactive area of the detector, e is the electron charge, and I_{dark} is the dark current.^{51,52} The specific detectivity at 3.11 THz is $D^* = 2.8 \times 10^{10}$ Jones (1 Jones = 1 cm Hz^{1/2} W⁻¹), signifying the good photodetection sensitivity of the 3D GFET photodetectors.

Figure 5 shows the radio frequency characteristics of the 3D GFET photodetectors as determined via impulse-response measurements. Optical pulses of 100 fs long (FWHM) at a wavelength of 633 nm and with pulse frequencies ranging from 50 to 700 kHz were produced using a pulsed diode laser (PDL 800-D, PicoQuant) and were focused on the devices through a polymethylpentene lens. The focused laser pulses had diameters of ~1 mm and pulse energy of 0.17 nJ at a repetition rate of 700 kHz. The impulse photocurrent signals from the 3D GFETs were first amplified using a low-noise current preamplifier (SRS70, Stanford Research Systems) with a bandwidth of 1 MHz and were then monitored using a 1 GHz bandwidth sampling oscilloscope (InfiniiVision DSO-X 3102T, Keysight). Because the frequencies of the voltage pulse signals that were monitored by the oscilloscope were exactly consistent with the frequencies of the incident optical pulses (Figure S15), the voltage pulse signals could be used to analyze the photoresponse

speed of the 3D GFET photodetectors. The rise and fall times are defined as the signal increases and decreases from 10% and 90% to 90% and 10% of the stable signal, respectively. From the impulse response of the 3D GFET photodetector (Figure 5a), the rise time (t_r) and the fall time (t_f) are 265 and 220 ns, respectively. A discrete-time Fourier transform of the time-domain data provided the spectrum of the 3D GFET photodetector, which is shown in Figure 5b. The 3 dB bandwidth of the 3D GFET photodetectors is 1.38 MHz, which is 5 orders of magnitude higher than that of graphene double-layer heterostructure photodetectors¹⁸ and 3 orders of magnitude higher than that of carbon nanotube–graphene hybrid photodetectors.¹⁷ Importantly, because the electrical bandwidth obtained is approximately the bandwidth of the measurement system, we anticipate that these 3D GFET photodetectors may also work at even higher frequencies. Table 1 summarizes the reported high-performance photodetectors based on graphene and other two-dimensional (2D) materials.^{12,13,16,18,40,43,47,51,53–56} Even though the 3D GFET photodetectors do not have the highest responsivity, the highest detectivity, the lowest NEP, or the fastest response speed, they have the broadest operation wavelength range and good comprehensive performances. For more comparison about the photoelectrical properties of the photodetectors based on 2D materials, one can refer to a recent review paper by Long et al.⁵⁷

In summary, self-rolled-up 3D GFETs can be used as high-performance photodetectors that have high photoresponsivity, broad spectral range, and high operating speed simultaneously. To promote further improvements in device performance, high-quality graphene and asymmetrical electrode structures should be used. The fabrication technique proposed in this paper can also be transferred to enable the fabrication of 3D photoelectronic devices and systems based on MoS₂, black phosphorus and other graphene-like 2D materials.

■ ASSOCIATED CONTENT

§ Supporting Information

The Supporting Information is available free of charge on the ACS Publications website at DOI: [10.1021/acs.nanolett.8b04099](https://doi.org/10.1021/acs.nanolett.8b04099).

Additional details on the fabrication process of the 3D GFETs, Raman spectra, carrier mobility and graphene–metal contact resistance, the gate leakage current of the 3D GFETs, GFET samples, scanning photocurrent measurement of the 3D GFETs, photoresponsivity enhancement, the gating effect dependent on Si substrate, the polarization dependence of photocurrent for the 3D GFETs, simulation of the optical field of the 3D GFETs, influence of the 3D GFET tube diameter to the photoresponsivity, temporal photoresponse characteristics, gate-voltage-dependent photoresponsivity of the 3D GFETs in the THz region, and radiofrequency characteristics of the 3D GFET photodetectors ([PDF](#))

■ AUTHOR INFORMATION

Corresponding Authors

*E-mail: dengtao@bjtu.edu.cn.

*E-mail: liuzw@tsinghua.edu.cn.

ORCID

Tao Deng: [0000-0001-9597-4833](https://orcid.org/0000-0001-9597-4833)

Yingxin Wang: [0000-0001-8230-5497](https://orcid.org/0000-0001-8230-5497)

Notes

The authors declare no competing financial interest.

ACKNOWLEDGMENTS

This research was supported by the National Natural Science Foundation of China (grant no. 61604009), the Fundamental Research Funds for the Central Universities (grant no. 2018JBM002), and the Beijing Municipal Natural Science Foundation (grant no. 4164095).

REFERENCES

- (1) Bonaccorso, F.; Sun, Z.; Hasan, T.; Ferrari, A. C. *Nat. Photonics* **2010**, *4*, 611–622.
- (2) Koppens, F. H. L.; Mueller, T.; Avouris, P.; Ferrari, A. C.; Vitiello, M. S.; Polini, M. *Nat. Nanotechnol.* **2014**, *9*, 780–793.
- (3) Xia, F.; Mueller, T.; Lin, Y. M.; Valdes-Garcia, A.; Avouris, P. *Nat. Nanotechnol.* **2009**, *4*, 839–843.
- (4) Mueller, T.; Xia, F.; Avouris, P. *Nat. Photonics* **2010**, *4*, 297–301.
- (5) Rao, G.; Freitag, M.; Chiu, H. Y.; Sundaram, R. S.; Avouris, P. *ACS Nano* **2011**, *5*, 5848–5854.
- (6) Mueller, T.; Xia, F.; Freitag, M.; Tsang, J.; Avouris, P. *Phys. Rev. B: Condens. Matter Mater. Phys.* **2009**, *79*, 245430.
- (7) Xu, X.; Gabor, N. M.; Alden, J. S.; van der Zande, A. M.; McEuen, P. L. *Nano Lett.* **2010**, *10*, 562–566.
- (8) Sun, D.; Aivazian, G.; Jones, A. M.; Ross, J. S.; Yao, W.; Cobden, D.; Xu, X. *Nat. Nanotechnol.* **2012**, *7*, 114–118.
- (9) Wang, F.; Zhang, Y.; Tian, C.; Girit, C.; Zettl, A.; Crommie, M.; Shen, Y. R. *Science* **2008**, *320*, 206–209.
- (10) Echtermeyer, T. J.; Britnell, L.; Jasnos, P. K.; Lombardo, A.; Gorbatchev, R. V.; Grigorenko, A. N.; Geim, A. K.; Ferrari, A. C.; Novoselov, K. S. *Nat. Commun.* **2011**, *2*, 455–458.
- (11) Fang, Z.; Liu, Z.; Wang, Y.; Ajayan, P. M.; Nordlander, P.; Halas, N. J. *Nano Lett.* **2012**, *12*, 3808–3813.
- (12) Pospischil, A.; Humer, M.; Furchi, M. M.; Bachmann, D.; Guider, R.; Fromherz, T.; Mueller, T. *Nat. Photonics* **2013**, *7*, 892–896.
- (13) Gan, X.; Shieh, R. J.; Gao, Y.; Meric, I.; Heinz, T. F.; Shepard, K.; Hone, J.; Assefa, S.; Englund, D. *Nat. Photonics* **2013**, *7*, 883–887.
- (14) Wang, X.; Cheng, Z.; Xu, K.; Tsang, H. K.; Xu, J. B. *Nat. Photonics* **2013**, *7*, 888–891.
- (15) Sun, Z.; Liu, Z.; Li, J.; Tai, G. A.; Lau, S. P.; Yan, F. *Adv. Mater.* **2012**, *24*, 5878–5883.
- (16) Ni, Z. Y.; Ma, L. L.; Du, S. C.; Xu, Y.; Yuan, M.; Fang, H. H.; Wang, Z.; Xu, M. S.; Li, D. S.; Yang, J. Y.; Hu, W. D.; Pi, X. D.; Yang, D. R. *ACS Nano* **2017**, *11*, 9854–9862.
- (17) Liu, Y.; Wang, F.; Wang, X.; Wang, X.; Flahaut, E.; Liu, X.; Shi, Y.; Zhang, R.; Li, Y.; Wang, X.; et al. *Nat. Commun.* **2015**, *6*, 9589.
- (18) Liu, C. H.; Chang, Y. C.; Norris, T. B.; Zhong, Z. *Nat. Nanotechnol.* **2014**, *9*, 273–278.
- (19) Furchi, M.; Urich, A.; Pospischil, A.; Lilley, G.; Unterrainer, K.; Detz, H.; Klang, P.; Andrews, A. M.; Schrenk, W.; Strasser, G.; Mueller, T. *Nano Lett.* **2012**, *12*, 2773–2777.
- (20) Engel, M.; Steiner, M.; Lombardo, A.; Ferrari, A. C.; Löhneysen, H. V.; Avouris, P.; Krupke, R. *Nat. Commun.* **2012**, *3*, 906.
- (21) Rogers, J.; Huang, Y.; Schmidt, O. G.; Gracias, D. H. *MRS Bull.* **2016**, *41*, 123–129.
- (22) Bhowmick, S.; Frost, T.; Bhattacharya, P. *Opt. Lett.* **2013**, *38*, 1685–1687.
- (23) Dastjerdi, M. H. T.; Mi, Z. *Electron. Lett.* **2014**, *50*, 680–682.
- (24) Wang, H.; Zhen, H.; Li, S.; Jing, Y.; Huang, G.; Mei, Y.; Lu, W. *Sci. Adv.* **2016**, *2*, No. e1600027.
- (25) Barcelos, I. D.; Moura, L. G.; Lacerda, R. G.; Malachias, A. *Nano Lett.* **2014**, *14*, 3919.
- (26) Deng, T.; Yoon, C. K.; Jin, Q.; Li, M.; Liu, Z.; Gracias, D. H. *Appl. Phys. Lett.* **2015**, *106*, 203108.
- (27) Grimm, D.; Bufon, C. C. B.; Deneke, C.; Atkinson, P.; Thurmer, D. J.; Schäffel, F.; Gorantla, S.; Bachmatiuk, A.; Schmidt, O. G. *Nano Lett.* **2013**, *13*, 213–218.
- (28) Froeter, P.; Yu, X.; Huang, W.; Du, F.; Li, M.; Chun, I.; Kim, S. H.; Hsia, K. J.; Rogers, J. A.; Li, X. *Nanotechnology* **2013**, *24*, 475301.
- (29) Chen, S.; Cai, W.; Chen, D.; Ren, Y.; Li, X.; Zhu, Y.; Kang, J.; Ruoff, R. S. *New J. Phys.* **2010**, *12*, 125011.
- (30) Lee, Y.; Bae, S.; Jang, H.; Jang, S.; Zhu, S.; Sim, S. H.; Song, Y. I.; Hong, B. H.; Ahn, J. H. *Nano Lett.* **2010**, *10*, 490–493.
- (31) Zang, J.; Ryu, S.; Pugno, N.; Wang, Q.; Tu, Q.; Buehler, M. J.; Zhao, X. *Nat. Mater.* **2013**, *12*, 321–325.
- (32) Xu, W.; Qin, Z.; Chen, C. T.; Kwag, H. R.; Ma, Q.; Sarkar, A.; Buehler, M. J.; Gracias, D. H. *Sci. Adv.* **2017**, *3*, No. e1701084.
- (33) Barcelos, I. D.; Marçal, L. A. B.; Deneke, Ch.; Moura, L. G.; Lacerda, R. G.; Malachias, A. *RSC Adv.* **2016**, *6*, 103707–103713.
- (34) Nagashio, K.; Nishimura, T.; Kita, K.; Toriumi, A. *Jpn. J. Appl. Phys.* **2010**, *49*, 051304.
- (35) Li, H. M.; Shen, T. Z.; Lee, D. Y.; Yoo, W. J. *IEDM* **2012**, 549–552.
- (36) Xia, F. N.; Golizadeh-Mojarad, R.; Freitag, M.; Lin, Y. M.; Tsang, J.; Perebeinos, V.; Avouris, P.; Mueller, T. *Nano Lett.* **2009**, *9*, 1039–1044.
- (37) Feng, Z. H.; Yu, C.; Li, J.; Liu, Q. B.; He, Z. Z.; Song, X. B.; Wang, J. J.; Cai, S. J. *Carbon* **2014**, *75*, 249–254.
- (38) Nath, A.; Kong, B. D.; Koehler, A. D.; Anderson, V. R.; Wheeler, V. D.; Daniels, K. M.; Boyd, A. K.; Cleveland, E. R.; Myers-Ward, R. L.; Gaskill, D. K.; Hobart, K. D.; Kub, F. J.; Jernigan, G. G. *Appl. Phys. Lett.* **2017**, *110*, 013106.
- (39) Park, J.; Ahn, Y. H.; Ruiz-Vargas, C. *Nano Lett.* **2009**, *9*, 1742–1746.
- (40) Long, M. S.; Gao, A. Y.; Wang, P.; Xia, H.; Ott, C.; Pan, C.; Fu, Y. J.; Liu, E. F.; Chen, X. S.; Lu, W.; Nilges, T.; Xu, J. B.; Wang, X. M.; Hu, W. D.; Miao, F. *Sci. Adv.* **2017**, *3*, No. e1700589.
- (41) Freitag, M.; Low, T.; Avouris, P. *Nano Lett.* **2013**, *13*, 1644–1648.
- (42) Lee, E. J. H.; Balasubramanian, K.; Weitz, R. T.; Burghard, M.; Kern, K. *Nat. Nanotechnol.* **2008**, *3*, 486–490.
- (43) Cai, X.; Sushkov, A. B.; Suess, R. J.; Jadidi, M. M.; Jenkins, G. S.; Nyakiti, L. O.; Myers-Ward, R. L.; Li, S.; Yan, J.; Gaskill, D. K.; Murphy, T. E.; Drew, H. D.; Fuhrer, M. S. *Nat. Nanotechnol.* **2014**, *9*, 814–819.
- (44) Guo, X. T.; Wang, W. H.; Nan, H. Y.; Yu, Y. F.; Jiang, J.; Zhao, W. W.; Li, J. H.; Zafar, Z.; Xiang, N.; Ni, Z. H.; Hu, W. D.; You, Y. M.; Ni, Z. H. *Optica* **2016**, *3*, 1066–1070.
- (45) Nanot, S.; Cummings, A. W.; Pint, C. L.; Ikeuchi, A.; Akiho, T.; Sueoka, K.; Hauge, R. H.; Leonard, F.; Kono, J. *Sci. Rep.* **2013**, *3*, 1335.
- (46) He, X. W.; Fujimura, N.; Lloyd, J. M.; Erickson, K. J.; Talin, A. A.; Zhang, Q.; Gao, W. L.; Jiang, Q.; Kawano, Y.; Hauge, R. H.; Leonard, F.; Kono, J. *Nano Lett.* **2014**, *14*, 3953–3958.
- (47) Mittendorff, M.; Winnerl, S.; Kamann, J.; Eroms, J.; Weiss, D.; Schneider, H.; Helm, M. *Appl. Phys. Lett.* **2013**, *103*, 021113.
- (48) Spirito, D.; Coquillat, D.; De Bonis, S. L.; Lombardo, A.; Bruna, M.; Ferrari, A. C.; Pellegrini, V.; Tredicucci, A.; Knap, W.; Vitiello, M. S. *Appl. Phys. Lett.* **2014**, *104*, 061111.
- (49) Tong, J.; Muthee, M.; Chen, S. Y.; Yngvesson, S. K.; Yan, J. *Nano Lett.* **2015**, *15*, 5295–5301.
- (50) Bauer, M.; Venckevicius, R.; Kasalynas, I.; Boppel, S.; Mundt, M.; Minkevicius, L.; Lisauskas, A.; Valusis, G.; Krozer, V.; Roskos, H. G. *Opt. Express* **2014**, *22*, 19235–19241.
- (51) Guo, N.; Gong, F.; Liu, J. K.; Jia, Y.; Zhao, S. F.; Liao, L.; Su, M.; Fan, Z. Y.; Chen, X. S.; Lu, W.; Xiao, L.; Hu, W. D. *ACS Appl. Mater. Interfaces* **2017**, *9*, 34489–34496.
- (52) Gong, X.; Tong, M.; Xia, Y.; Cai, W.; Moon, J. S.; Cao, Y.; Yu, G.; Shieh, C. L.; Nilsson, B.; Heeger, A. J. *Science* **2009**, *325*, 1665–1667.
- (53) Wang, G.; Zhang, M.; Chen, D.; Guo, Q. L.; Feng, X. F.; Niu, T. C.; Liu, X. S.; Liu, A.; Lai, J. W.; Sun, D.; et al. *Nat. Commun.* **2018**, *9*, 5168.
- (54) Xie, Y.; Zhang, B.; Wang, S.; Wang, D.; Wang, A.; Wang, Z.; Yu, H.; Zhang, H.; Chen, Y.; Zhao, M.; Huang, B.; Mei, L.; Wang, J. *Adv. Mater.* **2017**, *29*, 1605972.
- (55) Guo, Q.; Pospischil, A.; Bhuiyan, M.; Jiang, H.; Tian, H.; Farmer, D.; Deng, B.; Li, C.; Han, S.; Wang, H.; Xia, Q.; Ma, T.; Mueller, T.; Xia, F. *Nano Lett.* **2016**, *16*, 4648.

- (56) Tan, W. C.; Huang, L.; Ng, R. J.; Wang, L.; Hasan, D. M. N.; Duffin, T. J.; Kumar, K. S.; Nijhuis, C. A.; Lee, C.; Ang, K. W. *Adv. Mater.* **2018**, *30*, 1705039.
- (57) Long, M.; Wang, P.; Fang, H.; Hu, W. *Adv. Funct. Mater.* **2018**, *1803807*.